Resolving nonhydrostatic effects in oceanic lee waves

F.T. Mayer *, O.B. Fringer

The Bob and Norma Street Environmental Fluid Mechanics Laboratory, Department of Civil and Environmental Engineering, Stanford University, Stanford, CA 94305, USA

ARTICLE INFO

ABSTRACT

With increased computing power, the horizontal grid-spacing of regional ocean models is decreasing to the point where they can directly simulate lee waves. Although oceanic lee waves can be inherently nonhydrostatic, such as in the abyssal ocean or in the Gulf Stream, regional ocean models are frequently run in hydrostatic mode to avoid the computational expense of solving the nonhydrostatic pressure. However, the effects of the nonhydrostatic pressure and the numerical error on the accuracy of the simulated lee waves is not immediately obvious. To quantify these effects, this paper presents hydrostatic and nonhydrostatic simulations of an idealized lee wave over both linear and nonlinear height and varying length bathymetry utilizing a range of horizontal grid-spacings. We present an analysis of the numerical error arising from the discrete linear, stratified Euler equations to identify the numerically induced physics in lee wave simulations. As expected for the second-order accurate model, the numerical error in the lee wave drag decreases quadratically with respect to horizontal grid refinement, although the error arises from two primary sources. The first is related to discretization of the kinematic bottom boundary condition, which acts to decrease the lee wave drag. The second is related to discretization of the nonhydrostatic pressure, which acts to increase the drag. Together, the results offer a regional ocean modeler several cautionary notes for calculating and interpreting properties of simulated lee waves, namely, that a hydrostatic model can produce the correct form drag due simply to numerical error, and attempting to employ a nonhydrostatic model to correct for this error can require prohibitively fine grid resolution.

1. Introduction

Simulating certain types of internal gravity waves remains computationally challenging for ocean models. Chief among these perennially vexing oscillatory signals, at least in terms of potential abundance, is the lee wave, which occurs wherever a steady current with stable stratification interacts with bathymetry. The generation of a lee wave causes drag on the background flow, hereafter referred to as lee wave drag, which is hypothesized to significantly affect the fate of momentum and energy in the ocean (Legg, 2020; Nikurashin and Ferrari, 2011; Trossman et al., 2016).

For global ocean models with $O(10)$ km or coarser resolution, lee waves are a subgrid-scale phenomenon that must be parameterized. Regional ocean simulations, however, are capable of resolving lee waves in both the coastal and abyssal ocean (Caulfield et al., 2019). Recent examples include Nikurashin et al. (2014), Zheng and Nikurashin (2019), Klymak (2018), Gula et al. (2018), and Marez et al. (2020). Often, these studies employ hydrostatic simulations to avoid the computational expense of solving the 3-D elliptic equation for the nonhydrostatic pressure. For lee waves, the hydrostatic model is appropriate when the horizontal length scale of the bathymetry L_{hill} is much

longer than the wavelength of the lee wave λ_{lee}, which in typical oceanic conditions is $\lambda_{lee} = O(1)$ km. As demonstrated by linear theory, however, when the length of the bathymetry narrows to the same order as the lee wavelength, the nonhydrostatic pressure reduces the magnitude of the pressure anomaly in the lee wave and attenuates the drag. Therefore, simulations over nonhydrostatic bathymetry that neglect this nonhydrostatic effect risk over predicting the lee wave drag.

Resolving a lee wave often requires the dual constraints of both a fine enough horizontal grid-spacing to capture the horizontal gradients in the lee wave as well as the expensive computation of the nonhydrostatic pressure. Dimensional analysis suggests that both of these requirements should be directly related to the length scale of the bathymetry. This paper thus presents a set of hydrostatic and nonhydrostatic simulations of an idealized lee wave over sinusoidal bathymetries of hydrostatic and nonhydrostatic length scale with a range of horizontal grid-spacing ($L_{hill}/100 < \Delta x < L_{hill}/4$). The simulations offer a quantitative diagnosis of the resolution requirement and the importance of the nonhydrostatic effect over various length bathymetry. Additionally, this paper presents an analytical evaluation

---

of the discrete lee wave equations and identifies how the truncation error affects the physical system. Lastly, this paper offers a brief comparison of hydrostatic and nonhydrostatic lee wave simulations over nonlinear height bathymetry to demonstrate that the lessons learned in the linear regime apply also in the nonlinear regime.

This paper is organized as follows. In Section 2, we introduce an idealized lee wave and derive a dimensionless form of the lee wave drag predicted by linear theory. In Section 3, we describe our simulations and analyze a set of high resolution simulations. In Section 4, we present a derivation of the modified equivalent lee wave drag from the discrete PDEs and compare it to the drag observed in our simulations. In Section 5, we offer a brief analysis of nonlinear lee wave simulations. Finally, in Section 6 we conclude with suggestions for grid resolutions needed to resolve hydrostatic and nonhydrostatic lee waves.

2. Linear lee wave theory and parameter space

2.1. Dimensional analysis

An idealized lee wave can be generated by a flow with constant background horizontal velocity U and buoyancy frequency $N^2 = \frac{g}{\rho_0} \frac{\partial \bar{\rho}}{\partial z}$ over a sinusoidal bathymetry of height h_0 and length $L_{hill} = 2\pi/k$ (see Fig. 1). Sinusoidal bathymetry is chosen in part for the simplicity that it offers the analysis. But it also serves as a reasonable approximation of a ubiquitous small-scale bathymetric feature of the ocean floor, the abyssal hills (Goff and Arbic, 2010). Abyssal hills are strongly anisotropic, appearing as an expanse of periodic ridges aligned with the mid-ocean ridges where they are formed. Locally, their amplitudes are focused at dominant wavelengths, such that they are similar to a sinusoid.

Rotation is neglected under the assumption of large Rossby number, $Uk/f > 1$, where f is the Coriolis frequency. In the presence of rotation, this assumption fails first for the longer (more hydrostatic) hill lengths. For the most hydrostatic hill length considered in this study, this assumption is equivalent to $N/f \geq O(100)$ (see Fig. 8.10 in Gill (1982)), which, using a typical oceanic buoyancy scale $N = O(0.001)$ s^{-1}, is valid at latitudes smaller than approximately 15°. Steady lee wave theory demonstrates that as Uk approaches the rate of f, rotation changes the lee wave wavelength, slows the vertically propagating wave front, and diminishes the form drag (Gill, 1982). For $Uk \leq f$, propagating lee waves cannot exist and the steady-state drag vanishes, though the rotationally-evanescent lee wave response may still entail significant drag (Klymak, 2018). Thus rotation is likely an important element of most oceanic lee waves. However, as the goal of this paper is to identify numerical considerations when resolving nonhydrostatic effects in lee waves, the analytical clarity gained by ignoring rotation outweighs the potential cost in realism.

We also assume that the depth of the domain, D, is irrelevant, i.e. that the ratio of the current to the first-mode internal gravity wave speed satisfies $U/(ND) \ll 1$. In the deep ocean, where $D \approx 4$ km and typical abyssal values of velocity and buoyancy give $U/N \approx 100$ m, the assumption of infinite depth is very reasonable. In coastal regions, where $D \approx 1$ km, reflections of the lee wave from the surface or pycnocline might become important (Khatiwala, 2003).

With these assumptions, the idealized lee wave is characterized by the dimensional quantities U, N, h_0, and k. Choosing U and N to nondimensionalize h_0 and k, the governing nondimensional parameters are $J = Nh_0/U$ and $\epsilon = Uk/N$. J is a Froude number, indicating a ratio of perturbation advection speed within the wave to its group velocity, and serves as a measurement of the nonlinearity of the lee wave (Mayer and Fringer, 2017). In this study, we focus the numerical analysis on linear height bathymetry, implying $J \ll 1$. However, the results are applicable for all subcritical lee waves ($J < 1$), where the nonlinear effects on the lee wave drag are small (Nikurashin and Ferrari, 2010). The results are also applicable to nonlinear height bathymetry with $J = O(1)$, as demonstrated in Section 5. We note that, although much

of the lee wave literature focuses on supercritical height bathymetry, there are many abyssal hill regions with subcritical heights (see Fig. 9 in Nikurashin et al. (2014)).

We will refer to the second nondimensional number $\epsilon = Uk/N$ as the nonhydrostatic parameter, since it informs the degree of nonhydrostatic effects in the lee wave. Uk may be interpreted as the frequency of the bathymetric forcing on the flow, implying that ϵ is the ratio of this forcing rate to the buoyant response rate of the fluid, N. Equivalently, one can view ϵ as a ratio of the wavelength of the lee wave, $\lambda_{lee} = 2\pi U/N$ to the wavelength of the hill, $L_{hill} = 2\pi/k$. If the hill is very long, such that $\lambda_{lee} \ll L_{hill}$, then $\epsilon \ll 1$ and the wave is hydrostatic (Gill, 1982). However, in their study of the global energy flux into lee waves, Nikurashin and Ferrari (2011) report that, upon weighting by the energy flux, the average horizontal and vertical wavelength of oceanic lee waves are 2.5 km and 700 m, respectively, which implies $U/N = 107$ m (see Eq. (20)) and $\epsilon = 0.27$. Although not strongly nonhydrostatic, this value of ϵ still entails qualitative and quantitative differences between hydrostatic and nonhydrostatic simulations, as demonstrated in this paper.

Seen as a ratio of frequencies, ϵ is analogous to ω/N for internal tides, where ω is the tidal frequency, and the hydrostatic regime is defined by $\omega \ll N$. For internal tides, ω/N relates directly to the angle of the tidal beam such that, as the tidal frequency approaches the buoyancy frequency, the beam steepens toward the vertical. Internal tide simulations run in hydrostatic mode when $\omega \approx O(N)$ will under predict this beam steepening (Vitousek and Fringer, 2014). An analogous relationship exists between ϵ and the angle of the group velocity vector in a lee wave, as shown in Fig. 1 and discussed below.

As a final comment on ϵ, note the potentially counter-intuitive scaling of the horizontal length by k rather than L_{hill}. This choice results from recognizing that the quantity $\delta = U/N$ is the inverse of the lee wave wavenumber, N/U, while the lee wave wavelength is $\lambda_{lee} = 2\pi U/N$. If one were to use L_{hill} to scale the horizontal, one could use λ_{lee} to arrive at the same expression for the nonhydrostatic parameter,

$$\epsilon = \frac{\lambda_{lee}}{L_{hill}} = \frac{2\pi U}{N L_{hill}} = \frac{Uk}{N}. \tag{1}$$

It would not be correct, however, to form a nonhydrostatic parameter as $\delta/L_{hill} = U/(N L_{hill})$, because as we show below, this choice obscures by a factor of 2π the distinction between the propagating and evanescent regime given by $\epsilon = 1$. Although it is still true that a flow is hydrostatic when $U/(N L_{hill}) \ll 1$ (Baines, 1995), omitting the factor of 2π has resulted in some studies assuming nearly hydrostatic bathymetry ($\epsilon \approx O(0.1)$), when it is in fact strongly nonhydrostatic ($\epsilon \approx O(1)$) (e.g. Zheng et al., 2012; Gula et al., 2018; Marez et al., 2020). As we demonstrate below, this can result in over predictions of the lee wave drag.

Our quantity of interest in this paper is the form drag associated with a lee wave, F, which is the drag in units of force per unit length into the page shown in Fig. 1. Since a scale for F in terms of ρ_0, U, and N is $\rho_0 U^3 N^{-1}$, the nondimensional form drag must satisfy

$$\frac{F}{\rho_0 U^3 N^{-1}} = f(J, \epsilon). \tag{2}$$

2.2. Nondimensional equations

We separate the flow into its external and internal quantities such that $\mathbf{u}_{\text{total}} = U\mathbf{e}_x + \mathbf{u}$, $\rho_{\text{total}} = \bar{\rho}(z) + \rho$, and $p_{\text{total}} = \rho_0 \bar{p}(z) + \rho_0 p$. Under these definitions, the governing steady Euler equations, after employing the Boussinesq approximation, are given by

$$U\frac{\partial u}{\partial x} + \mathbf{u} \cdot \nabla u = -\frac{\partial p}{\partial x}, \tag{3}$$

$$U\frac{\partial w}{\partial x} + \mathbf{u} \cdot \nabla w = -\frac{\partial p}{\partial z} - \frac{\rho}{\rho_0} g, \tag{4}$$

$$U\frac{\partial \rho}{\partial x} + \mathbf{u} \cdot \nabla \rho = \frac{\rho_0 N^2}{g} w, \tag{5}$$
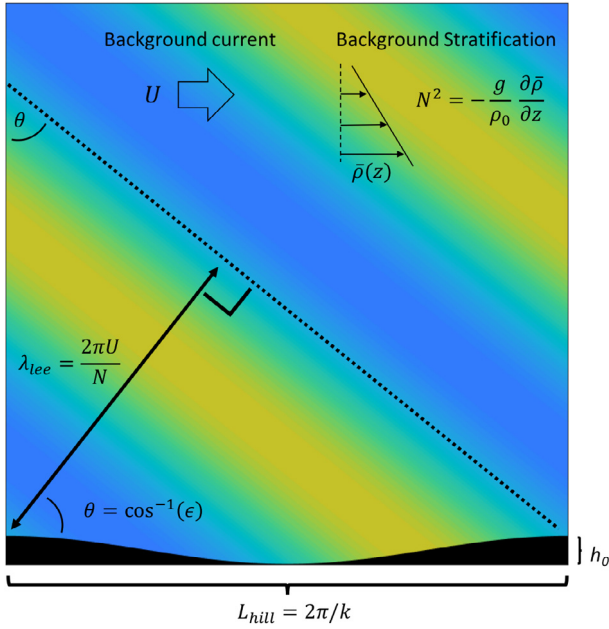
Fig. 1. A lee wave generated over sinusoidal bathymetry of length L_{hill} and height h_0 resulting from uniform background flow with horizontal velocity U and buoyancy frequency $N^2 = \frac{g}{\rho_0}\frac{\partial\bar{\rho}}{\partial z}$, where g is the gravitational constant, $\bar{\rho}$ is the background density of the fluid, and ρ_0 is the reference density. The color contours represent a linear wave-field variable, e.g. $u(x,z)$ (Eq. (26)). The dashed line indicates a line of constant phase in the wave field from the downstream crest. The lee wave wavelength, λ_{lee}, stretches perpendicularly from the phase line to the upstream crest, demonstrating the trigonometric relationship between the angle of the wavenumber vector and the horizontal, $\cos(\theta) = Uk/N \equiv \epsilon$. Note that θ is also the angle of the phase line to the vertical.

where $\nabla = \mathbf{e}_x \partial/\partial x + \mathbf{e}_z \partial/\partial z$, $N^2 = -g/\rho_0 \; \partial\bar{\rho}/\partial z$, subject to continuity $\nabla \cdot \mathbf{u} = 0$ and the kinematic boundary condition at $z = h(x)$

$$U\frac{\partial h}{\partial x} + u\frac{\partial h}{\partial x} = w, \tag{6}$$

where $h(x)$ is the topography as a deviation from a flat bottom and has a maximum crest to trough amplitude of h_0.

The equations are nondimensionalized using the inner variable scales defined by

$$[u,w,\rho,p,h,x,z] = \left[u_o u^*, w_0 w^*, R\rho^*, P p^*, h_0 h^*, k^{-1}x^*, \delta z^*\right], \tag{7}$$

where dimensionless quantities are indicated with the *. Using these scales, Mayer and Fringer (2017) show that the problem is uniquely characterized by $\epsilon = Uk/N$ and $J = Nh_0/U$, with the relevant inner scales (nondimensionalized by N and U)

$$\left[\frac{u_0}{U}, \frac{w_0}{U}, \frac{gR}{\rho_0 UN}, \frac{P}{U^2}, \frac{Nh_0}{U}, \frac{Nk^{-1}}{U}, \frac{N\delta}{U}\right] = \left[J, \epsilon J, J, J, J, \epsilon^{-1}, 1\right], \tag{8}$$

and governing nondimensional equations

$$\frac{\partial u^*}{\partial x^*} + J\mathbf{u}^* \cdot \nabla^* u^* = -\frac{\partial p^*}{\partial x^*}, \tag{9}$$

$$\epsilon^2\left(\frac{\partial w^*}{\partial x^*} + J\mathbf{u}^* \cdot \nabla^* w^*\right) = -\frac{\partial p^*}{\partial z^*} - \rho^*, \tag{10}$$

$$\frac{\partial\rho^*}{\partial x^*} + J\mathbf{u}^* \cdot \nabla^* \rho^* = w^*, \tag{11}$$

subject to $\nabla^* \cdot \mathbf{u}^* = 0$ and the kinematic bottom boundary condition

$$\left(1 + Ju^*\right)\frac{\partial h^*}{\partial x^*} = w^*. \tag{12}$$

Note that the vertical momentum equation (10) reduces to the hydrostatic balance when $\epsilon = 0$.

Upon inspection of the governing nondimensional equations, the equations are linearized by taking the $J \to 0$ limit, giving

$$\frac{\partial u^*}{\partial x^*} = -\frac{\partial p^*}{\partial x^*}, \tag{13}$$

$$\epsilon^2\frac{\partial w^*}{\partial x^*} = -\frac{\partial p^*}{\partial z^*} - \rho^*, \tag{14}$$

$$\frac{\partial\rho^*}{\partial x^*} = w^*. \tag{15}$$

Combining with $\nabla^* \cdot \mathbf{u}^* = 0$, one can rearrange these equations into a governing equation for w^*

$$\frac{\partial^2 w^*}{\partial z^{*2}} + \epsilon^2\frac{\partial^2 w^*}{\partial x^{*2}} + w^* = 0, \tag{16}$$

which is subject to the linearized bottom boundary condition

$$w^*(x^*,0) = \frac{\partial h^*}{\partial x^*}. \tag{17}$$

By linear superposition, any shape bathymetry can be decomposed into a sum of sinusoids with different wavelengths (Bell, 1975). Our interest is therefore in the solution for one such sinusoidal bathymetry, and we define a simple nondimensional height function as

$$h^*(x^*) = \frac{1}{2}\sin(x^*), \tag{18}$$

such that the nondimensional trough to crest height is unity.

When $\epsilon < 1$, the solution to Eq. (16) that satisfies the sinusoidal bottom boundary condition is of the form $w^*(x^*, z^*) = \cos(x^* + m^* z^*)$, which implies that the nondimensional vertical wavenumber

$$m^* = (1 - \epsilon^2)^{1/2}. \tag{19}$$

Dimensionalizing m^* with δ^{-1} (Eq. (8)), this results in a constant propagating lee wave wavenumber (Eq. 6.8.6 in Gill (1982))

$$K_{lee} = (m^2 + k^2)^{1/2} = N/U, \tag{20}$$

and lee wave wavelength

$$\lambda_{lee} = 2\pi \; K_{lee}^{-1} = 2\pi \; U/N. \tag{21}$$

Note that upon shifting to the frame of reference moving with the water, Eqs. (20) and (21) follow directly from the general dispersion relation for internal gravity waves in a continuous stratification, $\omega = \pm Nk/(k^2 + m^2)^{1/2}$, where the sinusoidal bathymetry propagating to the left at speed U acts as a forcing frequency $\omega = Uk$ (Pedlosky, 2003). In this reference frame, the group velocity vector has magnitude $\frac{U^2}{Nm} = U(1 - \epsilon^2)^{1/2}$ and is perpendicular to the wavenumber vector, in accordance with what is expected for internal gravity waves in continuous stratification. However, this is not the reference frame of most ocean simulations, and viewed in the frame of the hill, vector addition shows that the group velocity vector of the lee wave has magnitude

$$|c_g| = \epsilon U \tag{22}$$

and is parallel to the wavenumber vector, pointing downstream at an angle θ to the horizontal given by the relation (Eq. 6.8.13 in Gill (1982))

$$\epsilon = \cos(\theta) \tag{23}$$

(see also chapter 10 of Pedlosky (2003)). This implies that, as the wave becomes more nonhydrostatic ($\epsilon \to 1$), the wavenumber vector and the group velocity vector both tilt increasingly downstream ($\theta \to 0$). Lines of constant phase are perpendicular to the wavenumber vector, and thus make an angle θ to the vertical. This means that, as in internal tides, lines of constant phase point increasingly vertically with increasing nonhydrostasy. However, unlike internal tides, for the lee wave the energy propagates parallel to the wavenumber vector, and thus points increasingly horizontally with increasing nonhydrostasy. Note that this also implies the relation

$$\theta = \tan^{-1}\left(\frac{m}{k}\right) = \tan^{-1}\left(\frac{(1-\epsilon^2)^{1/2}}{\epsilon}\right), \tag{24}$$

which is indeed the inverse relation for an internal tide beam angle (Vitousek and Fringer, 2014).

In the hydrostatic limit, $k \to 0$, and the vertical wavenumber m asymptotes to the lee wave wavenumber, N/U. Thus, for hydrostatic simulations, where there is a finite k but the model nonetheless enforces the hydrostatic vertical wavenumber $m_{hs} = N/U$, the observed wavenumber vector will instead satisfy $K_{hs} = (k^2 + N^2/U^2)^{1/2}$, with a different angle of propagation given by

$$\theta_{hs} = \tan^{-1}\left(\frac{1}{\epsilon}\right). \tag{25}$$

Note that this relation is equivalent to the $\epsilon \ll 1$ limit of Eq. (24).

Substitution of $w^*(x^*, z^*) = \cos(x^* + m^* z^*)$ into the governing linear equations gives

$$u^*(x^*, z^*) = -\frac{1}{2}m^* \cos(x^* + m^* z^*), \tag{26}$$

$$w^*(x^*, z^*) = \frac{1}{2}\cos(x^* + m^* z^*), \tag{27}$$

$$\rho^*(x^*, z^*) = \frac{1}{2}\sin(x^* + m^* z^*), \tag{28}$$

$$p^*(x^*, z^*) = \frac{1}{2}m^* \cos(x^* + m^* z^*). \tag{29}$$

Note that in Eq. (26) and (29), the magnitudes of the horizontal velocity and pressure scale with $m^* = (1 - \epsilon^2)^{1/2}$, and are thus only $O(1)$ in the hydrostatic limit. This implies that although Mayer and Fringer (2017) derived Eq. (9)–(12) with the scaling $[u_0, P] = [JU, JU^2]$, a more general first-order scaling for u and p is $[u_0, P] = [JUm^*, JU^2m^*]$.

The form drag (per unit width) over one wavelength is given by

$$F_{nhs} = \int_0^{2\pi/k} p(x, z = 0)\frac{\partial h}{\partial x}\, dx, \tag{30}$$

where we use the sign convention of a positive drag acting to decelerate the flow. Nondimensionalizing gives

$$\frac{F_{nhs}}{\rho_0 U^3 N^{-1}} = J^2 \int_0^{2\pi} p^*(x^*, z^* = 0)\frac{\partial h^*}{\partial x^*}\, dx^*. \tag{31}$$

Substitution of p^* and h^* (Eqs. (18) and (29)) then gives, assuming $\epsilon < 1$,

$$\frac{F_{nhs}}{\rho_0 U^3 N^{-1}} = \frac{\pi}{4}J^2\left(1 - \epsilon^2\right)^{1/2}, \tag{32}$$

which shows that the nondimensional drag on the background current associated with lee waves grows in proportion to J^2, but decreases with increasing ϵ. The ϵ-dependence is a direct result of the factor m^* in the nonhydrostatic solution for the pressure anomaly (Eq. (29)). Despite the canonical status of this idealized lee wave in texts on stratified flows (Gill, 1982; Baines, 1995; Pedlosky, 2003), our derivation of the lee wave drag is unique in that the result is given in nondimensional form.

The momentum lost to the form drag results in a vertical momentum flux, $f_{flux} = \rho_0 u w$ away from the bathymetry. Nondimensionalizing with $\rho_0 U^2$ and inserting the propagating solution for u^* and w^* (Eqs. (26) and (27)), the nondimensional vertical momentum flux has the form

$$\frac{f_{flux}}{\rho_0 U^2} = -\frac{1}{4}J^2\,\epsilon\,m^*\,\cos^2(x^* + m^* z^*) = -\frac{f_0}{\rho_0 U^2}\,\cos^2(x^* + m^* z^*), \tag{33}$$

where the scale for the vertical momentum flux is

$$f_0 = \frac{1}{4}\rho_0 U^2 J^2 \epsilon m^*. \tag{34}$$

If we define some horizontal surface in (x, z) space that spans a single horizontal wavelength of the bathymetry, from $[0, 2\pi/k]$, the total momentum flux through this surface is

$$F_{flux} = -\int_0^{2\pi/k} f_{flux}\, dx = \frac{f_0}{k}\int_0^{2\pi} f_{flux}^*\, dx^*. \tag{35}$$

Substitution of Eq. (33) then gives

$$\frac{F_{flux}}{\rho_0 U^3 N^{-1}} = -\frac{1}{4}J^2 m^* \int_0^{2\pi} \cos^2(x^* + m^* z^*) dx^* \tag{36}$$

$$= -\frac{\pi}{4}J^2\left(1 - \epsilon^2\right)^{1/2}. \tag{37}$$

Thus, under our assumptions of linear height bathymetry and inviscid flow, the flux of momentum through any horizontal plane is equal and opposite to the form drag of the bathymetry on the flow, $F_{flux} = -F_{nhs}$ (Eq. 8.8.10 in Gill (1982)).

Finally, in the hydrostatic limit, $\epsilon \ll 1$, the lee wave drag (Eq. (32)) asymptotes to

$$\frac{F_{hs}}{\rho_0 U^3 N^{-1}} = \frac{\pi}{4}J^2. \tag{38}$$

This is the maximum drag that could possibly result from a single lee wave; the nonhydrostatic drag is always smaller by a factor of m^*, i.e.

$$F_{nhs} = m^* F_{hs} = (1 - \epsilon^2)^{1/2} F_{hs}. \tag{39}$$

F_{hs} therefore serves as a scale for drag in what follows. Note further that, because only the trough to crest height factors into the hydrostatic drag (Eq. (38)), any shape hill with a height h_0 will produce the same drag in the linear, hydrostatic limit. Indeed, even though we derived F_{hs} for a single sinusoidal hill, it is equivalent to the hydrostatic non-rotating drag given in Gill (1982), Eq. (8.8.20) for flow over an isolated bell shaped mountain. Although F_{hs} is the largest drag from a single hill, it does not produce the largest density of drag, given by $kF_{nhs}/(2\pi)$. Upon evaluating the derivative of $kF_{nhs}/(2\pi)$ with respect to the bathymetric wavenumber k, the largest drag density can be shown to occur for hills with horizontal wavenumber $k = N/(U\sqrt{2})$, or $\epsilon \approx 0.7$. Hence for a given area of ocean floor, a field of strongly nonhydrostatic hills can remove more momentum from the flow than would a single hydrostatic hill occupying the same horizontal span.

When $\epsilon \geq 1$, the solution to Eq. (16) is now of the form $w^*(x^*, z^*) = \cos(x^*)\exp(-m^* z^*)$, which implies $m^* = (\epsilon^2 - 1)^{1/2}$. Substitution into the governing linear equations gives

$$u^*(x^*, z^*) = \frac{1}{2}m^* \sin(x^*)\exp(-m^* z^*), \tag{40}$$

$$w^*(x^*, z^*) = \frac{1}{2}\cos(x^*)\exp(-m^* z^*), \tag{41}$$

$$\rho^*(x^*, z^*) = \frac{1}{2}\sin(x^*)\exp(-m^* z^*), \tag{42}$$

$$p^*(x^*, z^*) = -\frac{1}{2}m^* \sin(x^*)\exp(-m^* z^*). \tag{43}$$

Since the pairs $(p^*, \frac{\partial h^*}{\partial x^*})$ and (u^*, w^*) are now $\pi/2$ out of phase in x^*, the momentum flux and the lee wave drag are identically zero, giving

$$\frac{F_{nhs}}{\rho_0 U^3 N^{-1}} = 0 \tag{44}$$

when $\epsilon \geq 1$. Therefore, the background current is unaffected by steady flow over any small-amplitude hill narrower than the lee wave wavelength $\lambda_{lee} = 2\pi U/N$. In this regime, the vertical wavenumber m^* now increases with ϵ. As a consequence, with decreasing hill length, p^* and u^* grow in magnitude while shrinking in vertical scale to a thin layer above the hills. These are intrinsically nonhydrostatic processes and are impossible for hydrostatic simulations to capture.

Note that the bifurcation of the lee wave solution around $\epsilon = 1$ depends on the scaling of the horizontal length with k^{-1} rather than L_{hill}. If we had instead formed a nonhydrostatic parameter as $\frac{U}{N L_{hill}}$, as in Baines (1995), we would have obscured this separation of regimes by a factor of 2π. This has resulted in some studies mischaracterizing the hydrostasy of lee waves. For example, Gula et al. (2018) and Marez et al. (2020) simulate lee waves in the Gulf Stream launched by a chain of linear height seamounts with minimum lengths of from 1 to 2 km and background conditions $U/N \approx 100$ m (Zheng et al., 2012), such that the intuitive scaling gives $\frac{U}{N L_{hill}} = 0.01$–0.05, small values that imply hydrostatic behavior. As a result, the authors employed a

hydrostatic model to save computational resources. However, scaling with k^{-1} gives $\epsilon = \frac{Uk}{N} = 0.3–0.6$, larger values that, based on Eq. (39), suggest the true lee wave drag could be 5%–20% smaller than reported.

3. Simulations

3.1. Model set up

We employ two-dimensional (x-z) simulations with the nonhydrostatic SUNTANS model (Fringer et al., 2006). Because we consider only one-dimensional linear-height bathymetry and ignore rotation, the physics are symmetrical in the span-wise direction and there is no difference between two-dimensional and three-dimensional simulations. Indeed, even with strong rotation and nonlinear height one-dimensional bathymetry, Nikurashin et al. (2014) showed there is little difference between two- and three-dimensional lee wave simulations. For our simulations, boundary conditions are periodic in the horizontal, free-slip on the bottom and top, and the free surface is a rigid lid. All simulations begin at rest with uniform linear stratification such that the buoyancy frequency $N = 0.002$ rad s^{-1}. They are then spun up to a target velocity of $U = 0.2$ m s^{-1} using the adaptive forcing scheme of Nelson and Fringer (2017). This scheme nudges the flow with a uniform along-stream pressure gradient that is recomputed with each time step to enforce a constant volume-averaged horizontal velocity. The values of U and N are typical for the abyssal ocean (Nikurashin and Ferrari, 2011; Klymak, 2018) and coastal regions such as the Gulf Stream (Zheng et al., 2012), and set the characteristic vertical length scale to $\delta = U/N = 100$ m and the wavelength of the lee wave to $\lambda_{lee} = 2\pi\delta = 628$ m.

A primary goal of the simulations is to demonstrate the convergence of the lee wave drag to the linear theory in both hydrostatic and nonhydrostatic modes. As such, we simulate waves over idealized linear height bathymetry of sinusoidal shape, $h(x) = \frac{1}{2}h_0 \sin(kx)$. We keep the hill height fixed at $h_0 = 2$ m, but vary the hill length $L_{hill} = [4, 2, 1, 0.5]$ km. Since N and U are fixed, these bathymetric values give a linear height hill, with $J = 0.02$, and varying degrees of nonhydrostasy, with $\epsilon = [0.16, 0.32, 0.63, 1.26]$, which includes the evanescent regime with one hill satisfying $\epsilon > 1$. The bathymetry is represented as a piecewise linear function, referred to as cut cells (Zhang, 2017), rather than the discontinuous stair-stepping inherent to z-grids. This avoids both premature separation on the downslope as well as spurious evanescent waves from a stair-stepping bottom, and has been shown to provide much more accurate simulations of mountain waves (Adcroft et al., 1997). To test convergence, we vary the horizontal grid-spacing over $L_{hill}/100 < \Delta x < L_{hill}/4$, or equivalently, $0.06\,k^{-1} < \Delta x < 1.57\,k^{-1}$. To assess nonhydrostatic effects, the SUNTANS model is run in both hydrostatic and nonhydrostatic modes. The vertical resolution is held fixed (see below), and is chosen to accurately resolve the vertical scale, which is given by the vertical wavelength.

The depth in all simulations is $D = 7$ km, which is just over 11 lee wave wavelengths ($11\lambda_{lee} = 6912$ m). To avoid reflections from the surface, we use linear damping of perturbation horizontal velocity in a sponge layer that extends over the top 5 km of the domain. This is enforced with a source term on the right-hand side of the horizontal momentum equation of the form

$$S = -\frac{u - U}{\tau_s},$$

where

$$\tau_s = \frac{2\,\tau_0}{1 + \tanh[(z - z_s)/L_s]},$$

such that the strength of the damping smoothly transitions into the sponge layer beginning at distance above the floor $z_s = 2000$ m, with a decay length scale of $L_s = \frac{1}{2}\lambda_{lee} = 314$ m, and a minimum damping timescale of $\tau_0 = 4/N = 2000$ s. The vertical discretization employs a constant resolution of $\Delta z = 5$ m in the bottom 2 km of the domain,

and then stretching over the remaining 5 km such that, at the surface, $\Delta z_{top} = 300$ m. This is identical to the vertical grid in Nikurashin and Ferrari (2010). The vertical resolution near the bottom is $\Delta z = 5$ m, which is quite refined relative to the vertical scale of the lee wave of $\lambda_{lee} = 628$ m. Such high vertical resolution minimizes errors with respect to Δz, allowing us to focus on the nonhydrostatic effects dictated by convergence with respect to Δx.

All runs simulate 10 excitation periods, where the excitation period is given by $T_{ex} = L_{hill}/U$. In terms of the excitation period and the lee wave wavelength,

$$|c_g| = \epsilon U = \left(\frac{2\pi U}{L_{hill} N}\right) U = \left(\frac{2\pi U}{N}\right)\left(\frac{U}{L_{hill}}\right) = \frac{\lambda_{lee}}{T_{ex}}, \tag{45}$$

implying that in the hydrostatic limit, where the group velocity is directed vertically (Eq. (23)), the wave propagates upward by one wavelength for each excitation period. Because the excitation period scales with the length of the bathymetry, longer hills require longer simulation times. That is, for $L_{hill} = [0.5, 1, 2, 4]$ km and $U = 0.2$ m s^{-1}, $T_{ex} = [0.7, 1.4, 2.8, 5.6]$ hr, and $T_{sim} = [0.3, 0.6, 1.2, 2.3]$ days.

The kinematic viscosity is constant $\nu = 0.01$ m^2 s^{-1}, and no turbulence model is employed. Shakespeare and Hogg (2017) suggest that this value for ν is small enough to produce an effectively inviscid lee wave simulation. This is especially true for a lee wave with linear height bathymetry and a free-slip bottom boundary condition, in which there are no instabilities in the system to drive significant gradients. Indeed, test simulations with smaller viscosity produce little change in the measured lee wave drag. Ultimately, the choice of ν was driven by balancing stability considerations and a desire to avoid using an unreasonably small time step. These simulations employ second-order accurate central differencing for advection of momentum, which imposes the rather severe stability criterion on the size of the time step of $\Delta t \leq \frac{2\nu}{U^2} = 0.5$ s (assuming $(u_0, w_0) \ll U$). Hence, in all simulations we use $\Delta t = 0.1$ s.

3.2. Nonhydrostatic effects in resolved simulations

As derived above, the nonhydrostatic pressure in lee waves permits the wavenumber vector to orient such that its magnitude is always equal to N/U above variable wavenumber bathymetry (Eqs. (20) and (23)). In the hydrostatic limit ($\epsilon \to 0$), the wavenumber of the bathymetry effectively vanishes, and the wavenumber vector points vertically. As ϵ increases towards unity, the wavenumber vector tilts increasingly downstream, up to the limiting point in which the wavenumber of the bathymetry exactly equals the lee wave wavenumber, and the wavenumber vector points horizontally downstream. Beyond this limit, in which hills have wavenumbers larger than N/U ($\epsilon > 1$), there is no orientation in which the wavenumber vector can have magnitude N/U, and thus there is no propagating lee wave. This functional dependence of the angle of the nonhydrostatic wavenumber vector on ϵ is given by Eq. (24). In hydrostatic simulations, however, the vertical wavenumber remains fixed at its hydrostatic value, N/U, despite any variations in the wavenumber of the bathymetry. Hydrostatic simulations should thus produce a wavenumber vector with a different angle relative to the horizontal, given in Eq. (25). Furthermore, because the vertical wavenumber in hydrostatic simulations is insensitive to the wavenumber of the bathymetry, a hydrostatic model will still generate lee waves when $\epsilon > 1$. Well resolved nonhydrostatic and hydrostatic simulations of lee waves should display these diverging characteristics.

Fig. 2 shows output from the highest resolution nonhydrostatic simulations for each of the four hill lengths. The horizontal grid-spacing in each is the same relative to the wavelength of the hill, that is, $k\Delta x = 0.063$. The right panels in the figure show time series of the instantaneous wave drag over the course of the simulations nondimensionalized by F_{hs} (Eq. (38)). Note that all simulations begin by oscillating around the value F_{nhs} (Eq. (32)), with maximum values of $O(F_{hs})$. The period of these oscillations is precisely T_{ex}. From the
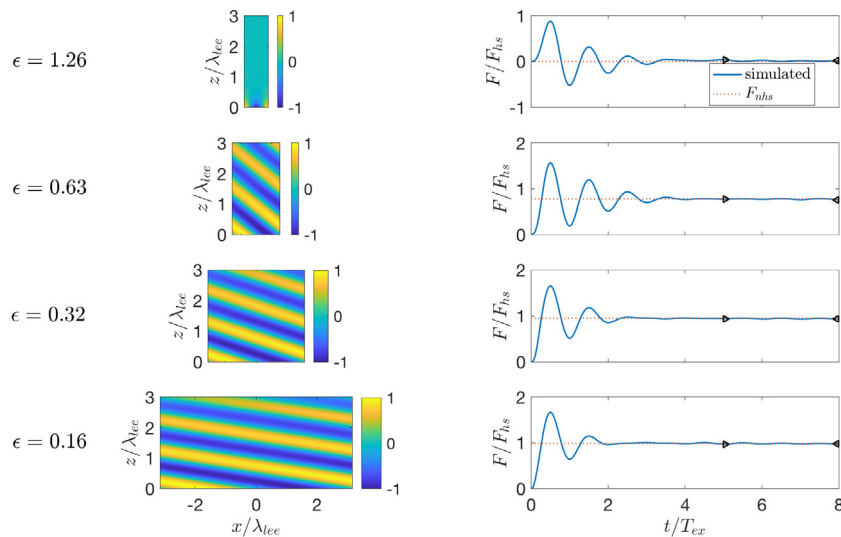
Fig. 2. Left: Average nondimensional perturbation horizontal velocity, $\overline{u}/(JUm^*)$ from high resolution $k\Delta x = 0.063$ simulations for each ϵ. The axes are nondimensionalized by the lee wave wavelength, λ_{lee}, and their aspect ratio is 1:1. The hill length increases from top to bottom as $L_{hill} = [0.5, 1, 2, 4]$ km ($\epsilon = [1.26, 0.63, 0.32, 0.16]$). Right: Drag nondimensionalized by F_{h_s} as a function of nondimensional time for each simulation. The dotted horizontal lines are the prediction from nonhydrostatic linear theory, i.e. F_{nhs}/F_{h_s}, and we note that $F_{nhs}/F_{h_s} = 0$ for $\epsilon > 1$. The triangles indicate the averaging period.

standpoint of dimensional analysis, this is not particularly surprising because, although there are two time scales in the problem arising from the terms N and U, only the latter of these relates to the forcing of the hill on the wave. Nevertheless, recognizing T_{ex} as the intrinsic lee wave time scale is an important observation from the standpoint of numerical modeling because it sets a lower bound on the necessary duration of a lee wave simulation. For these linear height hills, the oscillations decay within the first 3 to 4 excitation periods, and the measured wave drag asymptotes to F_{nhs}. Therefore, we define steady state as the period given by $5\,T_{ex} \leq t < 8\,T_{ex}$. In what follows, quantities with the overbar (e.g. $\overline{u}$) are time-averaged over this period.

The left panels in Fig. 2 display the average nondimensional perturbation horizontal velocity, $\overline{u}^* = \overline{u}/(JUm^*)$. Note that this nondimensionalization includes the nonhydrostatic factor $m^* = (1 - \epsilon^2)^{1/2}$ (as opposed to $u_0 = JU$ from Eq. (8)), and keeps the magnitude of the nondimensional perturbation $\overline{u}^*$ constant across ϵ. As predicted by nonhydrostatic linear theory, the lee wave wavelength is also constant when $\epsilon < 1$, and its orientation tilts downstream with increasing ϵ. Also in agreement with linear theory, the $\epsilon > 1$ length hill does not produce a propagating wave, and exerts almost no drag upon reaching equilibrium. Note, however, that even in this $\epsilon > 1$ case, the maximum instantaneous drag is of the same order as F_{h_s}. This occurs because it still requires work to establish the evanescent disturbance.

To offer a qualitative assessment of the role of nonhydrostatic pressure in these simulations, we show in the top panels of Fig. 3 the time-averaged vertical momentum flux, $\overline{f}(x, z) = \rho_0 \overline{u}(x, z)\overline{w}(x, z)$, nondimensionalized by f_0 (Eq. (34)) from the four nonhydrostatic simulations shown in Fig. 2. The bottom panels show the time-averaged flux from the equivalent hydrostatic simulations. As suggested by linear theory, the difference between the nonhydrostatic and hydrostatic models over the longest hill ($\epsilon = 0.16$; panels D and H) is imperceptible, while that over the narrowest hill ($\epsilon = 1.26$; panels A and E) is striking. Specifically, the hydrostatic simulation over the 0.5 km hill ($\epsilon = 1.26$; panel E) generates a propagating lee wave even though $\epsilon > 1$. Less striking, but still significant, is that the hydrostatic simulation above the 1 km hill ($\epsilon = 0.63$; panel F) retains a vertical periodicity of exactly the lee wave wavelength, λ_{lee}, while the nonhydrostatic simulation over this length hill (panel B) correctly permits the wavenumber vector to tilt downstream, leading to a longer vertical wavelength.

More quantitatively, Fig. 4 compares the angle of the simulated time-averaged wavenumber vector to the predictions from nonhydrostatic and hydrostatic theory (Eqs. (24) and (25)). The angle was

calculated by first determining the location of the maximum time-averaged vertical velocity as a function of z, which traces out a line of constant phase in the lee wave. We then perform a linear least-squares fit to determine the slope, and thus the angle of the line of constant phase to the vertical, which is equal to the angle of the wavenumber vector to the horizontal. As they are sufficiently resolved, both the simulated nonhydrostatic and hydrostatic wave angles agree with linear theory. Note that, because the evanescent nonhydrostatic simulation does not produce a propagating wave, it has a real k but an imaginary m, implying $\theta = 0$.

4. Effect of horizontal grid resolution

For an ocean model to resolve any type of wave, it requires horizontal grid-spacing fine enough to detect the horizontal gradients of said wave. Failure to satisfy this resolution requirement can result in numerically induced physics dominating the system. For example, when simulating solitary waves with a second-order accurate discretization, Vitousek and Fringer (2011) demonstrate that the horizontal gradients in the wave scale with the depth of the internal interface h_1, and thus the resolution must satisfy $\Gamma = \left(\frac{\Delta x}{h_1}\right)^2 \ll 1$ to avoid numerically induced dispersion reducing the speed of the solitary wave. Additionally Vitousek and Fringer (2011) show that the numerically induced dispersion can cause a hydrostatic simulation to correctly predict the speed and wavelength of a nonhydrostatic solitary wave, albeit for non-physical reasons. A similar analysis of the discrete lee wave system reveals that the horizontal gradients scale with the inverse bathymetric wavenumber k^{-1}, and that poor horizontal grid-spacing results in the model responding to a smaller effective bathymetric wavenumber, k_e, with a corresponding adjustment to the predicted lee wave drag.

To derive the analytical expressions for these numerically induced physics, we discretize the linear nondimensional steady lee wave equations (Eqs. (14)–(15)) and the nondimensional linear bottom boundary condition (Eq. (17)) using central differencing in space. As an illustrative example of the process, the second-order accurate in space discretization of the bottom boundary condition is given by

$$w_i^*(x^*, 0) = \frac{h_{i+1}^* - h_{i-1}^*}{2\Delta x^*}, \tag{46}$$

where the subscript i corresponds to the horizontal index of the grid point in the computational domain, and $\Delta x^* = (x_i^* - x_{i-1}^*) = k\Delta x$ is the
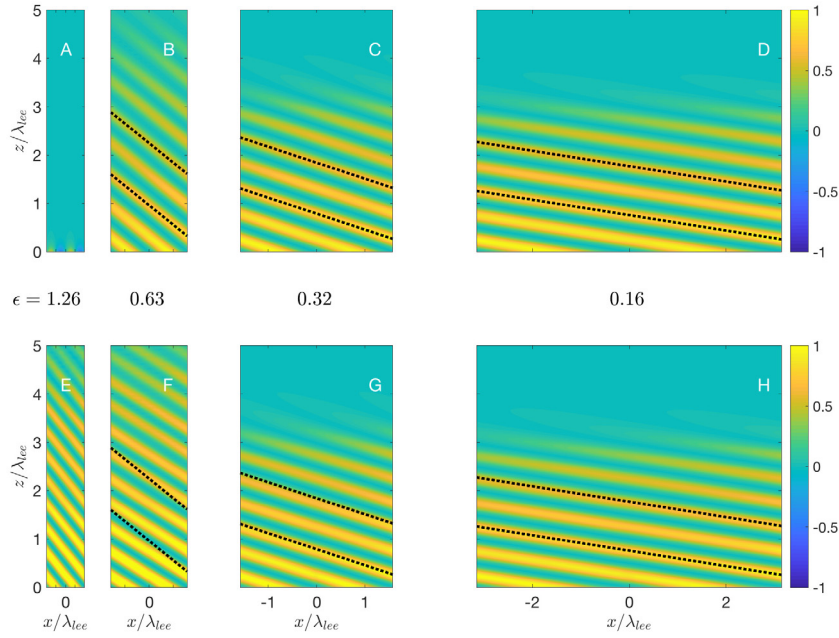
Fig. 3. Time-averaged vertical momentum flux $\overline{f}(x,z) = \rho_0 \overline{u}(x,z)\overline{w}(z,x)$, nondimensionalized by f_0 (Eq. (34)) for the nonhydrostatic (top) and hydrostatic (bottom) simulations. Black dotted lines in the $\epsilon < 1$ panels indicate lines of constant phase predicted by nonhydrostatic linear theory (Eq. (23)). As in Fig. 2, the aspect ratio is 1:1, but now the hill length increases from left to right, where again $L_{hill} = [0.5, 1, 2, 4]$ km ($\epsilon = [1.26, 0.63, 0.32, 0.16]$). The sponge layer is less effective with increasingly nonhydrostatic hills because it acts only on the perturbation horizontal velocity, which becomes a smaller component of the total perturbation velocity as the hills become narrow (see Eq. (26) and (27)).

nondimensional horizontal grid spacing. Expanding h^*_{i+1} and h^*_{i-1} with the Taylor series produces the modified equivalent form of the bottom boundary condition

$$w^*_e(x^*, 0) = \frac{\partial h^*}{\partial x^*} + \frac{\Delta x^{*2}}{6} \frac{\partial^3 h^*}{\partial x^{*3}} + O(\Delta x^{*4}), \tag{47}$$

where the subscript e reflects that this is the modified equivalent form of the expression from linear theory (Eq. (17)), and we have dropped the subscript i because the equations hold for all discrete space. Inserting the sinusoidal bathymetry $h^* = \frac{1}{2}\sin(x^*)$ implies the equivalent bottom boundary condition (accurate to $O(\Delta x^{*4})$)

$$w^*_e(x^*, 0) = \frac{1}{2}\left(1 - \frac{\Delta x^{*2}}{6}\right)\cos(x^*), \tag{48}$$

which is smaller in magnitude than the analytical solution for $w^*(x^*, 0)$ (Eq. (27)) by the factor $(1 - \frac{\Delta x^{*2}}{6})$. Discretizing the bottom boundary condition thus reduces the magnitude of the vertical velocity to one appropriate for a more hydrostatic hill length, implying that we can rewrite the modified equivalent bottom boundary condition as

$$w^*_e(x^*, 0) = \frac{1}{2}\frac{k_e}{k}\cos(x^*), \tag{49}$$

where

$$\frac{k_e}{k} = \left(1 - \frac{\Delta x^{*2}}{6}\right) \tag{50}$$

is the modified equivalent hill wavenumber. Recalling that the magnitude of the lee wave group velocity is equal to ϵU (Eq. (22)), the discrete bottom boundary condition effects a modified equivalent group velocity with magnitude

$$|c_{ge}| = \frac{k_e}{k}\epsilon U, \tag{51}$$

giving a modified equivalent group velocity that is slower than c_g by a factor of $(1 - \frac{\Delta x^{*2}}{6})$. This is analogous to numerical dispersion slowing the propagation of solitary internal waves in Vitousek and Fringer (2011).

Performing the same discretization on the linear Euler equations and cross differentiating gives the modified equivalent form of Eq. (16)

$$\frac{\partial w^{*2}_e}{\partial z^{*2}} + \epsilon^2 \frac{\partial w^{*2}_e}{\partial x^{*2}} + w_e = -\frac{\Delta x^{*2}}{6}\epsilon^2 \frac{\partial w^{*4}_e}{\partial x^{*4}} - \frac{\Delta z^{*2}}{6}\frac{\partial w^{*4}_e}{\partial z^{*4}} + O(\Delta x^{*4}, \Delta z^{*4}). \tag{52}$$

Note that, for a hydrostatic model, where $\epsilon = 0$, the error from the horizontal discretization vanishes. Assuming a solution of the form $w^*_e = \frac{1}{2}\frac{k_e}{k}\cos(x^* + m^*_e z^*)$ and $\Delta z^2 \ll \Delta x^2$ (since the vertical grid is very fine), the effective modified nondimensional vertical wavenumber to $O(\Delta x^4, \Delta z^2)$ is given by

$$m^*_e = \left(1 - \frac{k_e}{k}\epsilon^2\right)^{1/2}, \tag{53}$$

which is larger than the nonhydrostatic wavenumber (Eq. (19)), and thus more hydrostatic. The second-order accurate discretization of the linear Euler equations therefore induces another error that also has the effect of making the flow more hydrostatic. Indeed, at sufficiently coarse resolutions, even an evanescent length hill ($\epsilon \geq 1$) could generate a non-imaginary vertical wavenumber if $\frac{k_e}{k}\epsilon^2 < 1$. For example, a hill with $\epsilon = 1$ and $\Delta x^* = 0.5$ would have $\frac{k_e}{k} = 0.96$, and thus the effective vertical wavenumber $m^*_e = 0.2$. Note, however, that because F_e is only asymptotically accurate to $O(\Delta x^{*4})$, it is only strictly valid for resolutions in the asymptotic limit $\Delta x^{*4} \ll \Delta x^{*2}$.

Finally, following an identical derivation to that of the analytical wave drag (Eq. (32)), we arrive at the modified equivalent wave drag

$$F_e = \frac{k_e}{k}m^*_e F_{hs} = \left(1 - \frac{1}{6}(k\Delta x)^2\right)\left[1 - \epsilon^2\left(1 - \frac{1}{6}(k\Delta x)^2\right)\right]^{1/2} F_{hs}. \tag{54}$$

Expanding the square root, this gives

$$F_e = \left[1 - \frac{\epsilon^2}{2} - \frac{1}{6}(k\Delta x)^2 + \frac{\epsilon^2}{6}(k\Delta x)^2 + O\left((k\Delta x)^4, \epsilon^4\right)\right] F_{hs}. \tag{55}$$

Discretization of the lee wave system thus introduces two competing effects on the wave drag. First, the discrete bottom boundary condition causes an attenuation of the amplitude of the lee wave by the amount $\frac{(k\Delta x)^2}{6} F_{hs}$. Secondly, the nonhydrostatic discretization of the equations of motion results in an amplification of the vertical wavenumber, which in turn increases the magnitude of the form drag by approximately $\frac{\epsilon^2(k\Delta x)^2}{6} F_{hs}$. Only the first of these effects persists in the hydrostatic limit, or when using a hydrostatic model. However, in a coarsely resolved nonhydrostatic model over strongly nonhydrostatic bathymetry, the second effect is not negligible. Lastly, Eq. (54) offers an estimate of the resolution needed to achieve a desired precision. For example,

generating a hydrostatic lee wave with 96% of the theoretical wave drag requires $k\Delta x = (6 * (1 - .96)) = 0.5$, or $\Delta x = 0.08\,L_{hill}$. Although this conclusion simply confirms the general notion that resolving a physical phenomenon requires about ten grid points per length scale associated with that phenomenon, connecting the numerical error to the physics is nevertheless a novel pursuit. Indeed, as regional models increase their resolution to the point that they generate lee waves, this result provides a useful analytical prediction of the numerical effects they should expect.

To illustrate the numerical effects in linear lee waves, in Fig. 5 we show the simulated time-averaged wave drags and overlay the equivalent modified wave drag F_e (Eq. (54)) corresponding to each of the four hill lengths ($\epsilon = [.16, .32, .63, 1.26]$), as well as the hydrostatic equivalent modified wave drag, given by evaluating F_e with $\epsilon = 0$. The scaling of the axes in Fig. 5 causes the hydrostatic simulations (dashed lines) to collapse onto a single curve that converges to $\overline{F}/F_{hs} = 1$ and is very well approximated by the hydrostatic form of F_e (dotted magenta line) at grid resolution smaller than $k\Delta x = 0.8$. At coarser grid resolution, the asymptotic theory used to derive F_e is no longer valid, and the hydrostatic $\epsilon \geq 0.32$ simulations perform better than predicted by F_e. Although anticipated by both hydrostatic theory and F_e, it is nevertheless noteworthy that all of the hydrostatic simulations converge with grid refinement to the same hydrostatic lee wave drag (F_{hs}). This occurs because the hydrostatic simulations generate lee waves with vertical wavenumbers equaling the hydrostatic value $m = N/U$, and thus display waves with maximum perturbation pressure, which linear theory shows to be proportional to m (Eq. (29)). Likewise, the nonhydrostatic simulations converge to the predictions from nonhydrostatic theory, $\overline{F}/F_{hs} = (1 - \epsilon^2)^{1/2}$ (Eq. (39)), which follows from the same reasoning as in the hydrostatic result with the difference that in the nonhydrostatic model, the vertical wavenumber adjusts such that the magnitude of the wavenumber vector is a constant N/U (Eqs. (20) and (23)). This nonhydrostatic adjustment to the vertical wavenumber entails an attenuation in the perturbation pressure away from its maximum hydrostatic value, and an attendant attenuation of the wave drag. For all but the evanescent 500 m length hill ($\epsilon = 1.26$), the drag increases with grid refinement and is well approximated by F_e for $k\Delta x < 0.8$. Again, at coarser resolution, where F_e is not valid, the $\epsilon = 0.32$ and $\epsilon = 0.63$ simulations perform better than predicted by F_e.

The 500 m hill ($\epsilon = 1.26$) presents the most surprising, and from the standpoint of a modeler wishing to resolve lee waves, the most discouraging result. Beginning with the hydrostatic model, as in all of the hydrostatic simulations above longer hills, those above the 500 m hill exhibit a lee wave with a hydrostatic vertical wavenumber, and thus the full hydrostatic drag, F_{hs}. The hydrostatic model thus dramatically over predicts the drag compared to the nonhydrostatic result of the drag-free evanescent wave. And, as in all of the propagating length simulations, the predicted drag increases with increasing grid refinement, following the hydrostatic form of F_e. This implies that a hydrostatic ocean model will generate lee waves even when the horizontal scale of the bathymetry is less than the evanescent length, thus producing erroneous numerical drag that increases with grid refinement. The nonhydrostatic model, on the other hand, converges to the correct no-drag result with grid refinement. However, with coarser resolution, the nonhydrostatic model also incorrectly predicts a finite drag above the evanescent hill. Even with a reasonable resolution of $k\Delta x = 0.32$, or $\Delta x = 25$ m, the nonhydrostatic model predicts a drag of $0.08\,F_{hs}$. Although the modified equivalent wave drag F_e with $\epsilon = 1.26$ (dotted green line) indicates that the nonhydrostatic model will produce numerically induced wave drag when m_e is real, this requires the coarse resolution of $k\Delta x > 1.48$, a regime in which the asymptotic theory used to derive F_e is not appropriate. This suggests an alternative numerical effect not captured by our discretization analysis that dominates for simulations over evanescent hill lengths. Noting that the rate of convergence appears first order and that this is a strongly nonhydrostatic simulation, it is likely that the numerical effect derives
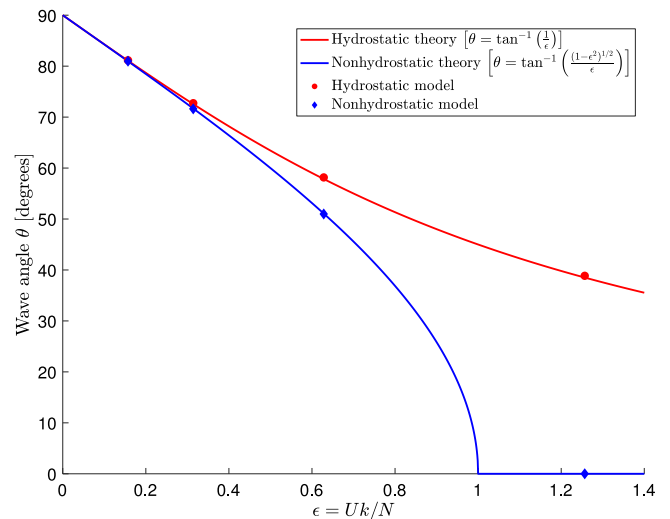

Fig. 4. The angle of the lee wave wavenumber vector with respect to the horizontal as a function of the nonhydrostatic parameter $\epsilon = Uk/N$. The theoretical curves are given in Eq. (24) (solid blue line) and Eq. (25) (solid red line) for nonhydrostatic and hydrostatic waves, respectively. The time-averaged wave angles measured in the $k\Delta x = 0.063$ simulations are plotted as blue diamonds and red circles for the nonhydrostatic and hydrostatic simulations, respectively. Note that the nonhydrostatic $\epsilon = 1.26$ gives $\theta = 0$ because the vertical wavenumber in the evanescent regime is imaginary.

from the bottom boundary condition on the nonhydrostatic pressure, which is not second order accurate with cut cells (Zhang, 2017). It is also possible that it results from the $O(\Delta z^{*2})$ term that we neglected in order to simplify the derivation of m_e (Eq. (53)). In any case, this study shows that, while the nonhydrostatic model significantly reduces the erroneous drag over evanescent length bathymetry, extremely high resolution is needed to eliminate it. For numerical studies focused on simulating the lee wave drag in a region dominated by linear height bathymetry, the best solution could be to low pass filter the bathymetry to remove evanescent length components, even when using a nonhydrostatic model. However, above less linear height bathymetry, there may be nonlinear interactions between evanescent and propagating components of the bathymetry, and low pass filtering the bathymetry might not be appropriate. Further research is required to determine the best course of action in this scenario. Nevertheless, this study suggests that simulating lee wave drag over narrow hills is a precarious business.

To emphasize the potential for over predicting the true drag with the hydrostatic model, in Fig. 6 we offer a rescaling of the time-averaged drag from the three $\epsilon < 1$ length hills, now nondimensionalizing by their respective values from nonhydrostatic linear theory, F_{nhs} (Eq. (32)). This plot does not show the evanescent case since the exact result is $F_{nhs} = 0$, which would yield $\overline{F}/F_{nhs} = \infty$. All nonhydrostatic results converge to $\overline{F}/F_{nhs} = 1$ and all hydrostatic results converge to $\overline{F}/F_{nhs} = (1 - \epsilon^2)^{-1/2}$. As observed in Fig. 5, the rates of convergence are well predicted by F_e when $k\Delta x < 0.8$, although for clarity, we do not show F_e here. For the 1 km hill ($\epsilon = 0.63$), the convergence of the hydrostatic model to F_{hs} implies that the over prediction in drag caused by using a high-resolution hydrostatic simulation asymptotes to 28%. On the other hand, using a nonhydrostatic model with coarser resolution over the same hill leads to an under prediction of the drag. Interestingly, because drag predicted by the hydrostatic model also decreases with coarser resolution, there exists a resolution where the two effects cancel, and the hydrostatic model gives better predictions of the nonhydrostatic drag than the nonhydrostatic model. For example, based on our simulations, the hydrostatic model with $\epsilon = 0.63$ would produce the correct drag ($\overline{F} = F_{nhs}$) when $k\Delta x = 1.32$, although the nonhydrostatic model would under predict the drag by 16% ($\overline{F} =$
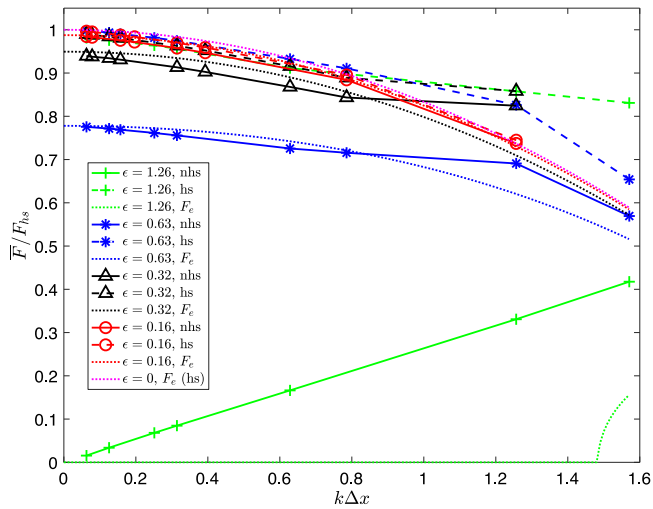
Fig. 5. Time-averaged drag nondimensionalized by hydrostatic linear theory, F_{hs} (Eq. (38)), as a function of nondimensional horizontal grid-spacing $\Delta x^* = k\Delta x$. The solid lines represent drag computed from nonhydrostatic simulations, while the dashed lines are from hydrostatic simulations. The markers along the lines indicate individual simulations, while the shape of the marker reflects the hill length of the simulation, where $[+, *, \triangle, \square]$ maps to $[0.5, 1, 2, 4]$ km ($\epsilon = [1.26, 0.63, 0.32, 0.16]$). The dotted lines represent the modified equivalent wave drag F_e/F_{hs} (Eq. (54)) for each ϵ, which is accurate to $O(\Delta x^{*4}, \Delta z^{*2})$. The hydrostatic form of F_e (dotted magenta line) results from evaluating F_e with $\epsilon = 0$.

Fig. 6. As in Fig. 5 but the *y*-axis is now scaled by F_{nhs} (Eq. (32)) and we only show the $\epsilon < 1$ simulations. The hatching indicates the region simulated in Klymak (2018), Gula et al. (2018), and Marez et al. (2020). and was computed using the modified equivalent wave drag F_e (Eq. (54)). The light blue asterisks at the intersections of the light blue dotted lines identify the resolutions at which the three hydrostatic models predict the correct nonhydrostatic drag. For the $\epsilon = [0.16, 0.32, 0.63]$ hills, these resolutions are $k\Delta x = [0.16, 0.41, 1.3]$. The purple asterisk identifies the predicted drag in the nonhydrostatic model with $\epsilon = 0.63$ at the resolution $k\Delta x = 0.16$, which is equal to $0.84F_{nhs}$.

$0.84F_{nhs}$) with this grid resolution. Note also that we can estimate this fortuitous resolution, which we will denote as Δx_{luck}, by equating the hydrostatic form of equation F_e (Eq. (54) with $\epsilon = 0$) to F_{nhs} (Eq. (32)), giving the relation

$$\Delta x^*_{luck} = \left[6 \left(1 - (1 - \epsilon^2)^{1/2} \right) \right]^{1/2}. \tag{56}$$

With $\epsilon = 0.63$, this predicts $\Delta x^*_{luck} = 1.16$, which is close to the observed value of $k\Delta x = 1.32$ even though this is much too coarse a resolution for F_e to be asymptotically valid. Running the hydrostatic model at this coincidental resolution is thus a case of getting the right answer for the wrong reason, and should not be taken as an endorsement for using coarse resolution hydrostatic models over nonhydrostatic bathymetry. Nevertheless, this analysis points to the folly of blindly refining the grid without considering the nonhydrostatic effect.

With this in mind, consider the hydrostatic simulations reported in Klymak (2018), Gula et al. (2018), and Marez et al. (2020), where $\Delta x \approx 100$ m, $\lambda_{lee} = \frac{2\pi U}{N} \approx 628$ m, and the minimum hill lengths were $L_{hill} \approx 1$–2 km, meaning $\epsilon \approx 0.3$–0.6 and $k\Delta x \approx 0.3$–0.6. Using F_e, we sketch this region in Fig. 6 with the cross hatch pattern. In this range of grid resolution, these simulations likely over predicted the drag from the narrowest components of their bathymetry by as much as 20%.

Although a hydrostatic simulation over nonhydrostatic bathymetry results in an over prediction of the drag, it is nevertheless significantly cheaper from a computational point of view. Fig. 7 displays the ratio of computation time required for otherwise identical simulations run with nonhydrostatic pressure (t_{nhs}) and without (t_{hs}). The nonhydrostatic SUNTANS model employs the block Jacobi preconditioner to solve the pressure-Poisson equation with the preconditioned conjugate gradient algorithm, which is less effective for increasing ϵ (Fringer et al., 2006). Thus, for a given resolution, the computational cost of a nonhydrostatic simulation increases with ϵ. For example, in the case of the strongly nonhydrostatic propagating length bathymetry ($L_{hill} = 1$ km, $\epsilon = 0.63$) with a resolution of $k\Delta x = 0.32$, it takes roughly five times as long to run in nonhydrostatic mode as in hydrostatic mode, while the same resolution over the most hydrostatic bathymetry ($\epsilon = 0.16$) is only twice as time consuming. However, because the $\epsilon = 0.16$ hill is practically hydrostatic, the difference between the hydrostatic and nonhydrostatic
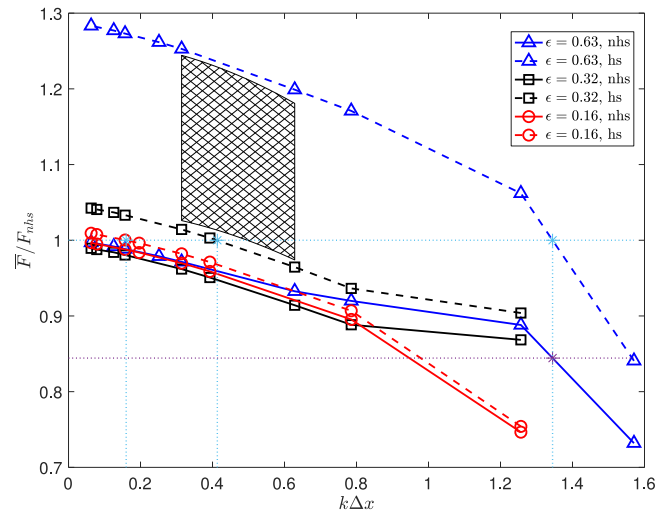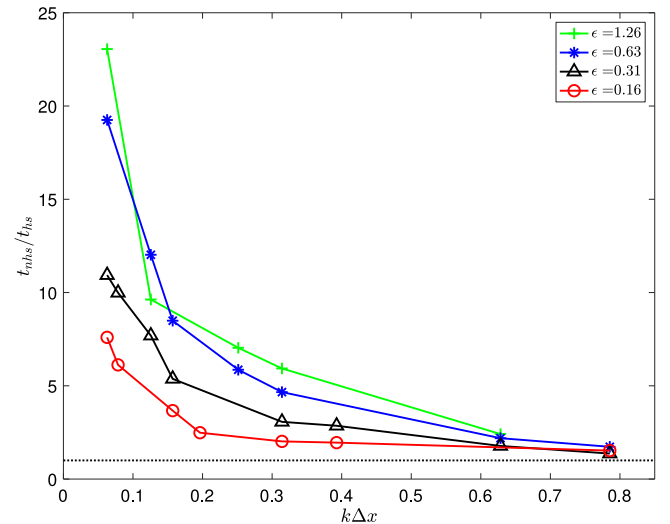

Fig. 7. Ratio of computation time for otherwise identical simulations run with (t_{nhs}) and without (t_{hs}) the nonhydrostatic pressure for different values of the nonhydrostatic parameter ϵ. The dotted black line indicates $t_{nhs}/t_{hs} = 1$. Run times from simulations coarser than $k\Delta x > 0.9$ are not shown.

drag is very small, i.e. $(F_{hs} - F_{nhs})/(F_{hs}) = (1 - m^*) = 0.013$, and thus there is little benefit to computing the nonhydrostatic pressure even if it is comparatively inexpensive. In addition to the increasing cost related to increasing ϵ, Fig. 7 also shows that for a given ϵ, the expense of a nonhydrostatic simulation increases dramatically with grid refinement. For example, with $\epsilon = 0.63$, the nonhydrostatic overhead is roughly two when $k\Delta x = 0.63$, and it increases to nearly twenty when $k\Delta x = 0.063$.

5. Application to nonlinear lee waves

Unlike the simulations in the previous sections, realistic abyssal hill bathymetry is often taller than U/N and generates nonlinear lee waves.
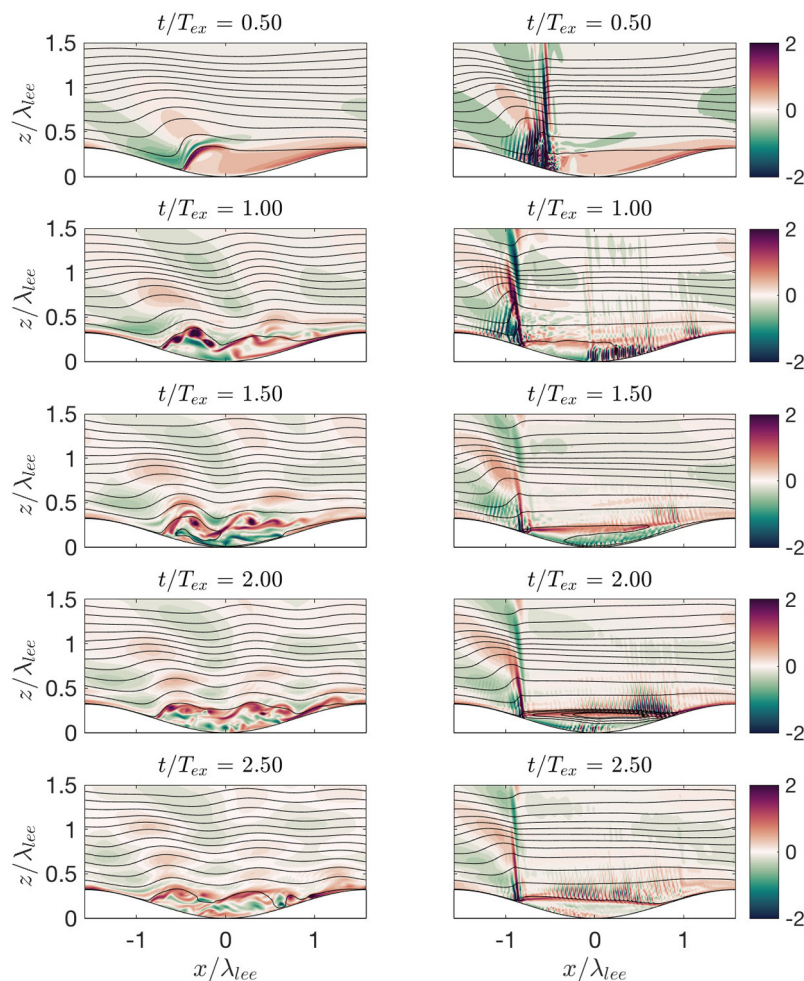
Fig. 8. Nondimensional vorticity ($\omega^* = \omega/(JN)$) and streamlines at half T_{ex} intervals for the nonhydrostatic (left column) and hydrostatic (right column) simulations with $J = 2$ and $\epsilon = 0.32$ ($h_0 = 200$ m, $L_{hill} = 2$ km). The colormap is 'curl' from Thyng et al. (2016).

In a separate paper, we present a series of high resolution nonhydrostatic lee wave simulations over nonlinear height ($J = O(1)$) sinusoidal bathymetry (Mayer and Fringer, 2020). The study reveals that for hills tall enough to cause blocking, wherein stagnant water becomes trapped in the valleys, the steady-state overtopping flow behaves as if flowing over a new bathymetry defined by the time-average lowest overtopping streamline (LOTS), whose height h_{eff} is always subcritical to the lee wave ($J_{eff} < 1$). Furthermore, we demonstrated that the lee wave drag can be computed by applying linear theory to the LOTS. The accuracy of the drag-measurement therefore depends on resolving the LOTS at appropriate scale for the associated linear lee wave, implying that the resolution requirements identified in this paper are applicable to nonlinear lee waves.

Mayer and Fringer (2020) identified two common nonhydrostatic features of the LOTS that can render the entire LOTS evanescent, even above bathymetry otherwise long enough to radiate lee waves. The first nonhydrostatic process, termed an "evanescent undulation", develops on the portion of the LOTS that separates the blocked layer from the overtopping flow. For the more hydrostatic hills, with $\epsilon < 0.5$, the streamline above the blocked layer develops a sinusoidal shape with a wavelength equal to λ_{lee}. Hence, if treated as bathymetry, this portion of the LOTS is evanescent, with $\epsilon = 1$, and does not contribute to the wave drag. The second nonhydrostatic component, "evanescent masking", results from the blocked layer filling in so much of the valley that the portion of the streamline still connected to the bathymetry shrinks in length, becoming shorter than λ_{lee}. In the presence of evanescent masking, the entirety of the LOTS is evanescent to the overtopping flow, and the wave drag vanishes.

Both of these phenomena are invisible to hydrostatic simulations. As a result, using a hydrostatic model with nonlinear-height periodic bathymetry can result in significant over predictions of the wave drag. To demonstrate as much, this section presents hydrostatic versions of the $J = 2$ simulations of Mayer and Fringer (2020) for the $\epsilon = [0.16, 0.32, 0.63]$ length hills. As in Mayer and Fringer (2020), the horizontal resolution of all simulations in this section is $\Delta x = 10$ m.

Fig. 8 shows snapshots of the nondimensional vorticity in the $L_{hill} = 2$ km simulation with and without nonhydrostatic pressure over the first 2.5 T_{ex}. Note the hydrostatic simulations generate a vertically-propagating lee wave with a narrow, grid-scale wavelength from the jump-like feature in the LOTS associated with its separation from the bathymetry. Downstream of the separation, the LOTS is relatively quiescent, showing no indication of evanescent undulations. The jump-like feature is similar to the result in Vitousek and Fringer (2011), in which hydrostatic simulations produce grid-scale solitary waves with numerical dispersion balancing the nonlinear steepening. It thus appears that, in the absence of nonhydrostatic dispersion needed to generate the evanescent undulations, the hydrostatic model produces a strong jump with a width of a few grid-spaces.

Fig. 9 shows the drag as a function of time for the $L_{hill} = 2$ km simulations in Fig. 8. We display two measurements of the drag: 1) the form drag, F_{form} (Eq. (30)), computed using the simulated pressure and the analytical bathymetry and 2) the wave drag, F_{flux} (Eq. (35)), computed by integrating the vertical momentum flux through a horizontal plane 15 m above the bathymetry. As shown in Mayer and Fringer (2020), the two measurements are identical when the lee wave reaches
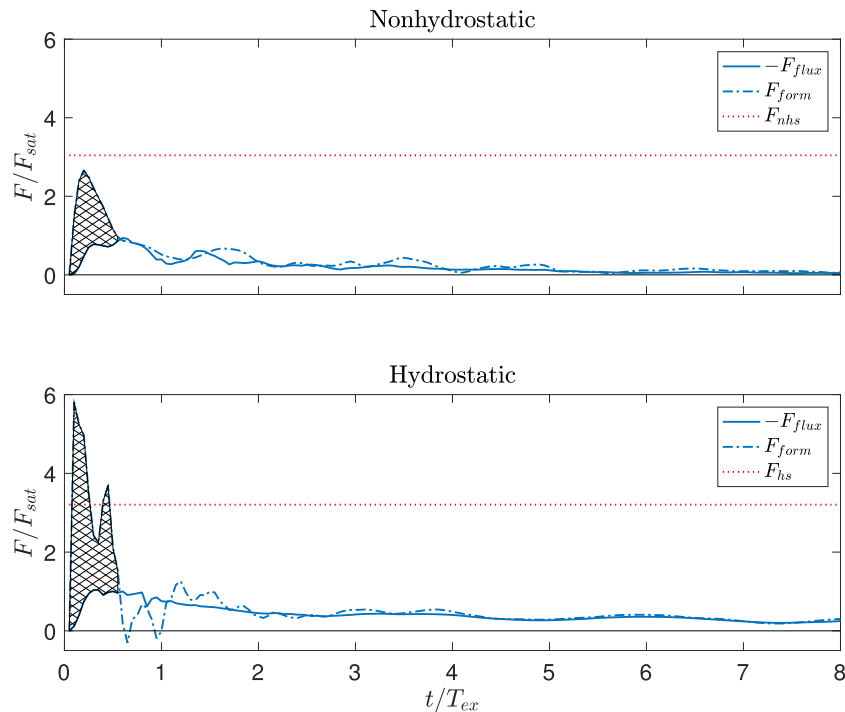
Fig. 9. Lee wave drag nondimensionalized by $F_{sat} = \rho_0 U^3 N^{-1}$ (Eq. (57)) as a function of time for the nonhydrostatic (top) and hydrostatic (bottom) simulations with $J = 2$ and $\epsilon = 0.32$ ($h_0 = 200$ m, $L_{hill} = 2$ km). Cross hatch pattern indicates local deposition of momentum during spin up.

steady state, indicating that all of the momentum removed from the background flow by the form drag is radiated away in the lee wave by the momentum flux. There is, however, a saturation limit to the momentum flux before a stably stratified fluid collapses into instability, approximated by Pierrehumbert (1987) as

$$F_{sat} = \rho_0 U^3 N^{-1}. \tag{57}$$

Indeed, in Fig. 9, both of the $L_{hill} = 2$ km simulations show the wave drag F_{flux} saturating at $O(F_{sat})$ within the first T_{ex} of the simulation. Any form drag larger than this saturation limit cannot radiate as momentum flux, and must therefore contribute to local changes in momentum. In Mayer and Fringer (2020), we demonstrate that for the spin up of supercritical lee wave simulations, the form drag is always momentarily much larger than the momentum flux, with a maximum close to the linear prediction F_{nhs}, because the form drag is temporarily acting to establish the blocked layer. This tendency is well represented in the nonhydrostatic $L_{hill} = 2$ km simulation of Fig. 9. The hydrostatic simulation also produces excess form drag during spin up. However, the time-series has two local maximums, with the first better approximated by twice the linear prediction for hydrostatic lee waves, $2 F_{hs}$. After the blocked layer stabilizes, both simulations show the form and wave drag coming into equilibrium. However, the hydrostatic simulation again produces more drag than its nonhydrostatic companion.

The hydrostatic over prediction of drag both in the spin-up phase and in the quasi-steady phase is a numerical artifact. It results from the hydrostatic simulation permitting the short length scale components of the LOTS to generate drag-producing lee waves, while the nonhydrostatic simulation correctly treats these features as evanescent. Fig. 10 shows the time-averaged vorticity for the six simulations. The three nonhydrostatic simulations (top panels) demonstrate the evanescent processes very well. The $L_{hill} = 1$ km simulation (top left) offers an especially satisfying demonstration of evanescent masking. And evanescent undulations above the blocked layer are evident for both the 2 km and the 4 km (top center and top right) hills. Faint lee waves can be seen propagating at an angle downstream from the beginning of the blocked layer, where the LOTS separates from the bathymetry. By contrast, all of the hydrostatic simulations (bottom panels) produce

a persistent vertically propagating lee wave from the beginning of the blocked layer. In the $L_{hill} = 1$ km simulation, the wave has an especially narrow horizontal wavelength, smaller than λ_{lee}, and is therefore not physical.

The time-averaged drag for these $\epsilon = [0.63, 0.32, 0.16]$ simulations is $\overline{F}_{nhs}/F_{sat} = [0.02, 0.06, 0.14]$ for the nonhydrostatic simulations and $\overline{F}_{hs}/F_{sat} = [0.12, 0.28, 0.29]$ for the hydrostatic simulations. Note there is very little difference in the drag between the hydrostatic $L_{hill} = 2$ km and 4 km simulations. This is because all the drag is generated by the narrow-width lee wave at the separation point; the rest of the blocked layer is flat. The hydrostatic model thus predicts a factor of $\overline{F}_{nhs}/\overline{F}_{hs} = [7.4, 4.6, 2.0]$ more drag than the nonhydrostatic models. Compared to the result from linear theory, in which the over prediction is given by $F_{nhs}/F_{hs} = (1 - \epsilon^2)^{1/2} = [1.29, 1.06, 1.01]$ (Eq. (39)), we see that the supercritical lee wave accentuates the nonhydrostatic effects, and linear theory serves as a lower bound for $\overline{F}_{hs}/F_{sat}$. Note that with $\Delta x/\lambda_{lee} = 0.016$, the nonhydrostatic models also over predict the drag in these simulations because they do not have enough resolution to generate fully evanescent lee waves, as demonstrated in Section 4. Thus, the ratio $\overline{F}_{hs}/\overline{F}_{nhs}$ offers a conservative estimate for how much a hydrostatic simulation of a $J = 2$ lee wave over predicts the lee wave drag. Even in the most hydrostatic of these simulations, with $\epsilon = 0.16$, the hydrostatic simulation produces twice as much drag as its nonhydrostatic counterpart, while in the linear regime, an $\epsilon = 0.16$-length hill should be well simulated by a hydrostatic simulation. Hence these nonlinear simulations offer further support for the general notion that lee waves are essentially nonhydrostatic features of ocean currents, and the ocean modeler is cautioned against treating them as otherwise.

6. Conclusion

In this paper, we derived a nondimensional form of the linear theory for lee wave drag above sinusoidal bathymetry and used SUNTANS with and without the nonhydrostatic pressure to demonstrate the convergence to theory of wave drag in simulated lee waves above bathymetry of linear height ($J \ll 1$) and varying length ($\epsilon = [0.16, 0.32, 0.63, 1.26]$).
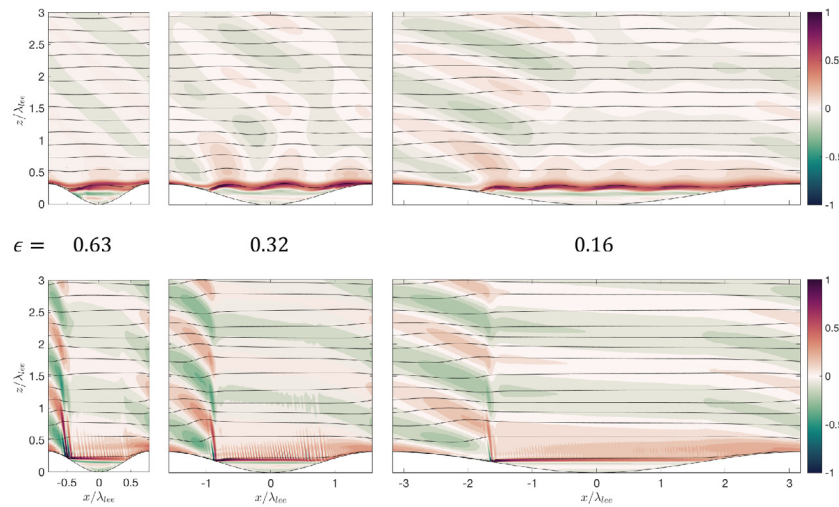
Fig. 10. Time-average nondimensional vorticity ($\overline{\omega}^* = \overline{\omega}/(JN)$) and streamlines for nonhydrostatic (top) and hydrostatic (bottom) supercritical simulations with $J = 2$. As in Fig. 3, the aspect ratio is 1:1 and the hill length increases from left to right, where $L_{hill} = [1, 2, 4]$ km ($\epsilon = [0.63, 0.32, 0.16]$).

Using central differencing in space, we derived a modified equivalent form of the steady lee wave drag, F_e (Eq. (54)), accurate to $O(\Delta x^{*4}, \Delta z^{*2})$, where $\Delta x^* = k\Delta x$ and $\Delta z^* = \frac{N}{U}\Delta z$, which shows that discretizing the lee wave system results in two forms of numerically induced physics, one effecting the magnitude of the group velocity vector, and the other its direction. Both of these numerically induced physics can be viewed as making the wave more hydrostatic, and yet they have opposite effects on the magnitude of the lee wave drag. The primary source of numerical physics results from the discretization of the bottom boundary condition, which results in a modification of the lee wave drag by the factor $k_e/k = 1 - \frac{1}{6}(k\Delta x)^2$. We observed that F_e correctly predicted the convergence of our numerical simulations to the predictions of linear theory for $k\Delta x < 0.8$, meaning that F_e offers a good estimate of the precision of a lee wave simulation such that, for example, achieving 96% accuracy requires $k\Delta x < 0.5$, or about $\Delta x = 0.08 L_{hill}$. In both the abyssal ocean and coastal regions such as the Gulf Stream, typical bathymetry that generates lee waves has horizontal length scales of O(km) (Goff and Arbic, 2010; Zheng et al., 2012). Resolving the resulting lee wave drag thus requires horizontal grid-spacing of $\Delta x = O(100\ m)$.

At the finest resolutions in this study, $k\Delta x = 0.063$, the lee waves display wavenumber vectors that agree with those predicted by linear theory. Specifically, in the nonhydrostatic model, the pressure allows the magnitude of the wavenumber vector to remain fixed at N/U, thus requiring the vertical component of the wavenumber vector to decrease as $m = \frac{N}{U}(1 - \epsilon^2)^{1/2}$. In the hydrostatic model, however, the vertical component of the wavenumber vector remains fixed at the value given by the hydrostatic limit, $m_{hs} = N/U$, irrespective of the wavenumber of the bathymetry. Over nonhydrostatic bathymetry, this implies that hydrostatic models generate larger magnitude pressure perturbations than dynamically required, resulting in an over prediction of the wave drag. Our simulations demonstrate that this over prediction converges to that predicted by the comparison of hydrostatic and nonhydrostatic linear theory, $F_{nhs} = m^* F_{hs}$, where $m^* = (1 - \epsilon^2)^{1/2}$. Additionally, for evanescent length hills ($\epsilon > 1$), the nonhydrostatic drag vanishes, $F_{nhs} = 0$, which is in stark contrast to hydrostatic simulations above evanescent hills, which still generate a hydrostatic lee wave, producing the full hydrostatic drag, F_{hs}.

At coarser resolutions, for all but the nonhydrostatic model above the evanescent bathymetry, the computed drags were lower than those predicted by theory in accordance with F_e. Therefore, coarsely resolved hydrostatic simulations can produce the "correct" nonhydrostatic drag, but for the wrong reason. On the other hand, for the nonhydrostatic model above evanescent bathymetry, the coarser resolution simulations

generate significant drag even though it should vanish. Indeed, even at a resolution of $\Delta x = 25$ m ($k\Delta x = 0.32$), the nonhydrostatic model still predicts drag of $O(0.1)\ F_{hs}$. This is a particularly unwelcome discovery as it suggests that both hydrostatic and nonhydrostatic simulations of stratified flow over evanescent length bathymetry will produce numerically induced lee waves unless they employ spectacularly fine resolution.

Finally, in the supercritical ($J > 1$) regime with periodic bathymetry, where blocking results in wave-drag saturation, we showed that hydrostatic lee wave simulations dramatically over predict the drag, even above hydrostatic-length bathymetry, due to a non-physical representation of the blocked layer.

As a whole, this paper has demonstrated that resolving lee waves requires the dual constraint of very fine horizontal grid-spacing and computation of the nonhydrostatic pressure. Failure to satisfy the resolution requirement generally results in a moderate under prediction of drag, while failure to compute the nonhydrostatic pressure results in an over prediction of the drag, which is negligible above hydrostatic-length and linear-height bathymetry, but becomes dramatic as $\epsilon \to 1$ or $J > 1$. Satisfying both of these constraints is computationally expensive. In cases where the nonhydrostatic pressure is important, the time required to run a sufficient resolution nonhydrostatic model was found to be about five times that of an otherwise identical hydrostatic model. However, above nonhydrostatic length bathymetry ($\epsilon \geq O(0.1)$), this paper demonstrates that choosing only to improve resolution without also computing the nonhydrostatic pressure amounts to doing more work for a wrong answer.

CRediT authorship contribution statement

F.T. Mayer: Validation, Formal analysis, Investigation, Data curation, Writing- original draft, Visualization. **O.B. Fringer:** Conceptualization, Methodology, Software, Resources, Writing- review & editing, Supervision, Project administration, Funding acquisition.

Declaration of competing interest

The authors declare that they have no known competing financial interests or personal relationships that could have appeared to influence the work reported in this paper.

Acknowledgments

References

Adcroft, A., Hill, C., Marshall, J., 1997. Representation of topography by shaved cells in a height coordinate ocean model. Mon. Weather Rev. 125 (9), 2293–2315.

Baines, P., 1995. Topographic Effects in Stratified Flows. Cambridge University Press, Cambridge.

Bell, T.H., 1975. Topographically generated internal waves in the open ocean. J. Geophys. Res. 80 (3), 320–327.

Caulfield, C.-c.P., Sutherland, B., Achatz, U., Klymak, J., 2019. Recent Progress in Modelling Imbalance in the Atmosphere and Ocean. American Physical Society.

Fringer, O.B., Gerritsen, M., Street, R.L., 2006. An unstructured-grid, finite-volume, nonhydrostatic, parallel coastal ocean simulator. Ocean Model. 14 (3), 139–173.

Gill, A., 1982. Atmosphere-Ocean Dynamics. Academic Press, San Diego.

Goff, J.A., Arbic, B.K., 2010. Global prediction of abyssal hill roughness statistics for use in ocean models from digital maps of paleo-spreading rate, paleo-ridge orientation, and sediment thickness. Ocean Model. 32 (1), 36–43.

Gula, J., Lahaye, N., Marez, C., Blacic, T., 2018. Generation of waves and vortices in the lee of the Charleston Bump. In: Paper Presented At the Meeting of NHOM-Brest: Workshop on Non-Hydrostatic Ocean Modeling: Bridging the Gap Between Sub-Mesoscales and Boundary Layer Turbulence, Brest, France.

Khatiwala, S., 2003. Generation of internal tides in an ocean of finite depth: analytical and numerical calculations. Deep Sea Res. I: Oceanograph. Res. Pap. 50 (1), 3–21.

Klymak, J.M., 2018. Nonpropagating form drag and turbulence due to stratified flow over large-scale abyssal hill topography. J. Phys. Oceanogr. 48 (10), 2383–2395.

Legg, S., 2020. Mixing by oceanic lee waves. Annu. Rev. Fluid Mech. 53.

Marez, C.D., Lahaye, N., Gula, J., 2020. Interaction of the Gulf Stream with small scale topography: a focus on lee waves. Sci. Rep. 10 (1), 1–10.

Mayer, F.T., Fringer, O.B., 2017. An unambiguous definition of the froude number for lee waves in the deep ocean. J. Fluid Mech. 831.

Mayer, F.T., Fringer, O.B., 2020. Improving nonlinear and nonhydrostatic ocean lee wave drag parameterizations. J. Phys. Oceanogr. 50 (9), 2417–2435.

Nelson, K., Fringer, O., 2017. Reducing spin-up time for simulations of turbulent channel flow. Phys. Fluids 29 (10), 105101.

Nikurashin, M., Ferrari, R., 2010. Radiation and dissipation of internal waves generated by geostrophic motions impinging on small-scale topography: Theory. J. Phys. Oceanogr. 40 (5), 1055–1074.

Nikurashin, M., Ferrari, R., 2011. Global energy conversion rate from geostrophic flows into internal lee waves in the deep ocean. Geophys. Res. Lett. 38 (8), 1–6. http://dx.doi.org/10.1029/2011GL046576.

Nikurashin, M., Ferrari, R., Grisouard, N., Polzin, K., 2014. The impact of finite-amplitude bottom topography on internal wave generation in the Southern Ocean. J. Phys. Oceanogr. 44 (11), 2938–2950.

Pedlosky, J., 2003. Waves in the Ocean and Atmosphere: Introduction to Wave Dynamics. Springer Science & Business Media.

Pierrehumbert, R., 1987. An essay on the parameterization of orographic gravity wave drag. In: Seminar/Workshop on Observation, Theory and Modelling of Orographic Effects. Seminar: 15-19 September 1986, Workshop: 19-20 September 1986, vol. 1. ECMWF, Shinfield Park, Reading, pp. 251–282, https://www.ecmwf.int/node/11673.

Shakespeare, C.J., Hogg, A.M., 2017. The viscous lee wave problem and its implications for ocean modelling. Ocean Model. 113, 22–29.

Thyng, K.M., Greene, C.A., Hetland, R.D., Zimmerle, H.M., DiMarco, S.F., 2016. True colors of oceanography: Guidelines for effective and accurate colormap selection. Oceanography.

Trossman, D.S., Arbic, B.K., Richman, J.G., Garner, S.T., Jayne, S.R., Wallcraft, A.J., 2016. Impact of topographic internal lee wave drag on an eddying global ocean model. Ocean Model. 97, 109–128. http://dx.doi.org/10.1016/j.ocemod.2015.10.013.

Vitousek, S., Fringer, O.B., 2011. Physical vs. numerical dispersion in nonhydrostatic ocean modeling. Ocean Model. 40 (1), 72–86.

Vitousek, S., Fringer, O.B., 2014. A nonhydrostatic, isopycnal-coordinate ocean model for internal waves. Ocean Model. 83, 118–144.

Zhang, Y., 2017. Numerical modeling for hydrodynamics and suspended sediment transport in estuarine marshes (Ph.D. thesis). Stanford University, Civil and Environmental Engineering Department.

Zheng, Q., Holt, B., Li, X., Liu, X., Zhao, Q., Yuan, Y., Yang, X., 2012. Deep-water seamount wakes on SEASAT SAR image in the gulf stream region. Geophys. Res. Lett. 39 (16).

Zheng, K., Nikurashin, M., 2019. Downstream propagation and remote dissipation of internal waves in the Southern Ocean. J. Phys. Oceanogr..